A Direct Numerical Simulation Investigation of the One-Phase Flow in a Simplified Emulsification Device

Peyman Olad
Department of Food Technology,
Engineering and Nutrition,
Lund University,
Lund SE-221 00, Sweden
e-mail: peyman.olad@food.lth.se

Marco Crialesi Esposito
Flow Centre,
Department of Engineering Mechanics,
Royal Institute of Technology (KTH),
Stockholm SE-100 44, Sweden
e-mail: marcoce@kth.se

Luca Brandt
Flow Centre,
Department of Engineering Mechanics,
Royal Institute of Technology (KTH),
Stockholm SE-100 44, Sweden
e-mail: luca@mech.kth.se

Fredrik Innings
Tetra Pak Processing Systems,
Department of Food Technology,
Engineering and Nutrition,
Lund University,
Lund SE-221 00, Sweden
e-mail: Fredrik.Innings@tetrapak.com

Andreas Håkansson
Department of Food Technology,
Engineering and Nutrition,
Lund University,
Lund SE-221 00, Sweden
e-mail: andreas.hakansson@food.lth.se

A Direct Numerical Simulation Investigation of the One-Phase Flow in a Simplified Emulsification Device

More detailed investigation of the flow inside emulsification devices, e.g., High-pressure homogenizers (HPHs) helps the industry to broaden the fundamental understanding of the working principle of these machines which in turn will pave the road to increase the breakup efficiency of emulsification processes. Direct numerical simulation (DNS) is not deemed as a practical method in industry due to the high computational cost and time. This study is the first DNS carried out on a model of an emulsification device model. The goal of this study is to set a benchmark for future CFD investigations using industrially favorable tools (RANS, LES, etc.). A scale-up model HPH is designed and the results show a successful modeling of the flow field mimicking the flow behavior inside a typical HPH. [DOI: 10.1115/1.4053896]

1 Introduction

High-pressure homogenizers (HPHs) are widely used unit operations in food-, pharma-, bioprocess-, and general chemical processing. Although also used for general dispersion and cell breakup, the most common application is breaking up oil droplets in oil-in-water emulsions (e.g., in fat globule breakup for dairy processing). Despite having been used industrially for well over 100 years, the fundamental mechanism of drop breakup in HPHs is still not completely understood and the thermodynamic efficiency of the process is exceedingly low. Obtaining a deeper fundamental understanding of the turbulent flow field is therefore an important step toward improved design.

In principle, an HPH consists of a high-power piston pump forcing the fluid through a narrow valve at high velocities (up to 100–200 m/s). The HPH valve consists of an inlet chamber (converging at the end), a narrow gap ($h \sim 50 - 150\mu$m), and an expanding outlet chamber. Figure 1(*a*) shows a schematic (not-to-scale) view of an industrial HPH valve. The general outline of the HPH valve flow has been studied experimentally using particle image velocimetry (PIV) in previous studies [1,2]. As the fluid exits the gap, it creates a turbulent jet that attaches to the wall some gap heights downstream. A large recirculation vortex is created above the jet, in the chamber outlet (see Fig. 1(*a*)). This presses down on the jet, decreasing its spreading rate. Experimental single drop breakup visualization studies [3–5] have shown disperse phase breakup at approximately 10–20 gap heights downstream of the exit, inside the turbulent jet.

The precise mechanism of turbulent drop breakup in the HPH jet is still disputed, which makes predictions more difficult. Some studies discussing turbulent HPH breakup assume that it is controlled by the dissipation rate of turbulent kinetic energy (TKE) [6–8] or the amount of turbulent energy in a specific range of eddy lengthscales. Mutsch et al. [9] argues that a combination of laminar deformation inside the HPH valve gap and turbulence in the outlet chamber leads to the breakup of the droplets. There is disagreement even at the general level on what turbulent property of the flow contributes to the breakup phenomenon. Solsvik et al. [10] carried out a literature review concluding that six breakage criteria have been proposed in the literature based on turbulent properties of the flow showing a lack of consensus. Thus, to obtain an agreement on the dominant mechanism of breakup, a fundamental understanding of the breakup process is needed which in turn requires a detailed understanding of both the characteristic HPH jet itself and the turbulent characteristics in the breakup region. Some advances have been made toward such an understanding using 2D-PIV [1,2,5] and RANS-CFD [8,11–13]. However, these techniques have some clear limitations. An experimental approach such as PIV cannot get close to the resolution required to capture the smallest temporal and spatial scales. Also, the nature of RANS CFD models leads them to provide less accuracy both due to the modeling of turbulent features as well as grid resolution. Detailed results for the dissipation rate of TKE will be quite useful for the studies on the breakup of droplets as others have suggested [6–8]. Turbulence as a 3D phenomenon could not be entirely captured by a 2D-PIV approach. This

Contributed by the Fluids Engineering Division of ASME for publication in the Journal of Fluids Engineering. Manuscript received June 2, 2021; final manuscript received December 21, 2021; published online March 11, 2022. Assoc. Editor: Lucy Zhang.

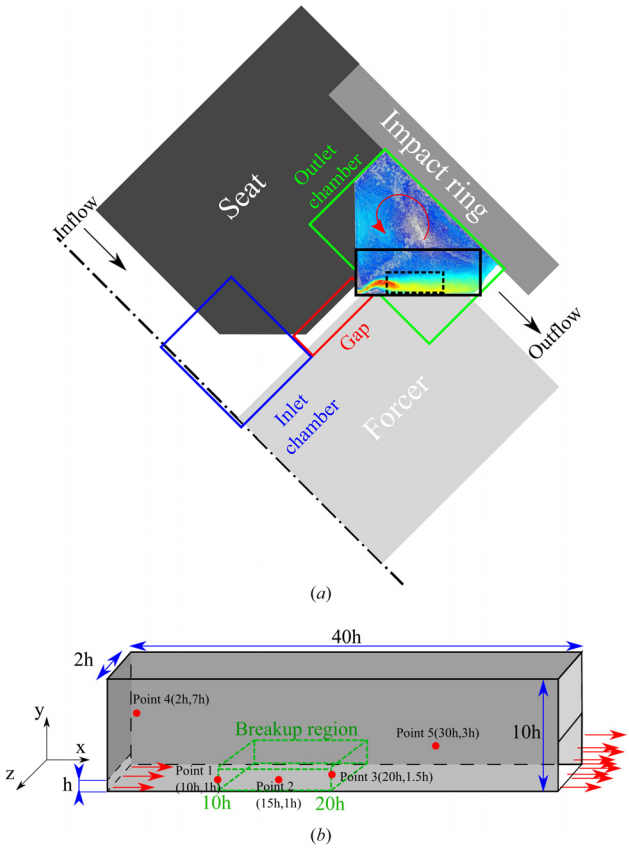

Fig. 1 (*a*) Schematic (not-to-scale) view of a generic industrial HPH valve with a typical instantaneous flow field inside the outlet chamber from [1]; As a rough illustration of the relevance of the simplified domain in the current study, the black box inside the outlet chamber represents the schematic shape of the DNS domain and the smaller dashed box shows the approximate position of the breakup region of interest, (*b*) Schematic view of the simplified outlet chamber as the computational domain for our DNS study (Points 1–5 are the positions where the convergence of the results is checked in Sec. 3.5)

includes the computation of the dissipation rate field which requires 3D information of the velocity field.

A direct numerical simulation (DNS), on the other hand, covers all possible spatial and temporal turbulent scales, i.e., no turbulence modeling is applied to the problem. This would provide superior, comprehensive, unprecedented accurate information on the flow field in an industrial machine such as homogenizer valves. The resolution of the flow field information goes down to the dissipative Kolmogorov scales, which is difficult to achieve by experimental methods such as PIV. DNS, however, is often limited to moderate operational speed and often relies on simplifying boundary conditions, e.g., periodicity in some spatial direction.

A large number of detailed investigations of turbulent wall jets can be found in the fluid dynamics literature starting with [14] who carried out experimental investigations to describe the general behavior of a wall-jet including mean velocity profiles and spreading rate. Since then, various experimental studies investigated wall-jet flows, mainly varying Reynolds numbers and expanding the investigations to higher flow statistics [15–23]. Launder et al. [24] present an extensive review on the studies on wall-jet flows carried out before the 1980s. More recently, high-fidelity numerical simulations, e.g., LES and DNS, have been used to investigate wall-jets. Dejoan and Leschziner [25] performed one of the first LES studies on plane wall jet comparing the results with previous experimental studies. This study was followed by several others [26–28]. Relatively fewer DNS studies have been carried out on wall-jet flows [29–31].

Nonetheless, the HPH jet of interest for turbulent drop break deviates from the jets investigated in these previous investigations: (i) the flow above the jet is heavily confined (see Fig. 1(*a*)) resulting in the characteristic vortex pressing down and influencing the HPH-jet spreading, (ii) the main interest in an applied setting is the region where drop breakup has been seen to occur rather than the self-similar region of the jet and these two may or may not coincide; and (iii) the Reynolds numbers in HPH cover a wider interval than the available DNS data. The long-term objective of this project is to improve the fundamental understanding of drop breakup in HPHs with the approach of combining DNS and experimental single drop breakup visualizations in a geometry similar to the effective region of drop breakup in an HPH valve. As a first step, this contribution aims to describe the single-phase turbulent flow of the HPH jet obtained by a DNS with special attention to the region where breakup has been seen to occur in previous investigations.

2 Model Geometry and Flow Case

The objective of this study is to perform a DNS describing the turbulent flow in conditions as close as possible to those in an industrially relevant HPH valve. The long-term objective is to extend the DNS investigations to two-phase simulations and compare the findings to experimental drop breakup visualizations and measurements. Thus a scaled-up model must be designed that both allows for a domain that is simple enough for implementing a computationally efficient DNS (i.e., as cuboidal as possible) and that have velocities and length-scales that allows for experimental investigations using high-speed cameras (the gap velocity in an industrial HPH valve can be above 150 m/s [32]). To achieve this, a number of practical limitations should be taken into account:

(1) The droplets and gap height h should be sufficiently large to make the visualization and photography possible in future experimental work.
(2) The gap bulk velocity, U_j, should be such that we can capture the breakup process through high-speed photography.
(3) Reduce the Reynolds number to make the DNS practical.
(4) The geometry should be as simple as possible to simplify the DNS and avoid further numerical complications.

As seen in Fig. 1(*a*), the HPH valve jet exits into a confined space and has attached to the wall before reaching the point where the drop breakup is expected. Thus, a confined wall jet provides a relevant representation of the actual flow, see Fig. 1(*b*). The distance between the attachment wall and the upper wall in the HPH valve is approximately 40 h, whereas a smaller value is used in this study ($Ly = 10$h) to reduce computational costs. The spanwise domain size is set to $Lz = 2$h. To mimic the confinement above the wall-attached jet, which creates a recirculation vortex interacting with the jet in an industrial HPH chamber [1] (see Fig. 1(*a*)), half of the outlet is a solid wall facing the inlet (see Fig. 1(*b*)). Therefore, the walls above the jet (Fig. 1(*b*)) closely mimic the outlet chamber confined by the impact ring and the seat in Fig. 1(*a*). A similar recirculation vortex designated with a circular red vector in Fig. 1(*a*) is generated inside the DNS domain (as it will be illustrated and discussed in Fig. 6). The black box inside the outlet chamber in Fig. 1(*a*) represents the schematic shape of the DNS domain (Fig. 1(*b*)) to better illustrate the relevance of the simplified HPH outlet chamber of the current study to a real outlet chamber of an industrial HPH. Furthermore, the dashed black box is a rough representation of the expected breakup region.

In designing a scaled-up model, one should ensure that the model properly represents the actual physical phenomenon. In order to do so, geometrical, kinematic, and dynamic similarities should exist between the model and the actual setup.

As Innings et al. [4] concludes, having a full dynamic similarity between the model and an industrial HPH valve is hardly achievable due to conflicting constraints. However, industrial HPHs are available in widely different sizes (operating at between 8500L/h

Table 1 Most important dimensionless numbers compared for the three cases of production-scale, pilot-scale, and scale-up HPH model

	Production- and pilot-scale HPH working span	Scale-up model
Properties and dimensions		
Gap height (h) (μm)	15–150	750
Initial drop size (d) (μm)	5	250
Gap bulk velocity (U_j) (m/s)	150	16
Dimensionless numbers		
Reynolds number (Re)	1700–26000	2100
h/η	90–690	100
d/L	0.01–0.11	0.11
d/η	23–30	34
δ_{99}/h	0.08–0.98	0.29
d/h	0.03–0.33	0.33

and 120L/h [1,32]. The difference in the relevant dimensionless numbers are therefore rather large (see Table 1), whereas emulsification experiments reveal that the underlying dynamics and process efficiency are similar [32,33]. Thus, a good scaling can be obtained by making sure that all relevant dimensionless numbers are within the range of these different HPH valve scales (cf. [4]).

The gap-based bulk Reynolds number, the gap height to the Kolmogorov length-scale, and the gap boundary layer thickness to gap height have previously been identified as important factors for achieving the correct one-phase flow scaling. When aiming to study breakup in the future, the Weber number (indicative of breakup in the turbulence inertial regime), Capillary number (indicative of breakup in the turbulent viscous regime), and the ratio between the initial drop size, gap height, integral length scale, and Kolmogorov length-scale should also scale accordingly. This was ensured by choosing the settings in Table 1.

3 Direct Numerical Simulation Methodology

3.1 Direct Numerical Simulation Code. An in-house DNS code is used in this study which has been validated in various studies [34–36]. A uniform Cartesian grid is used with the flow variables stored in staggered arrangements, where the vector fields are stored at the cell faces and scalar fields at cell centers. Spatial derivatives are computed using a second-order central differences scheme. We employ an Adams-Bashforth scheme for time discretization, ensuring 2nd order of accuracy. To impose the incompressibility condition and obtain a solenoidal velocity field, we solve at each time-step a constant coefficient Poisson equation. Such equation is solved using the direct FFT solver from [37], hence forcing a 2D domain-decomposition. More details on the numerical methods used can be found in Ref. [35].

The outlet chamber of the scale-up model (shown in Fig. 1(*b*)) is chosen as the domain for the DNS study. The dimensions of the domain are $L_x/h = 40$, $L_y/h = 10$, $L_z/h = 2$, where h is the gap height. The mesh is uniform in all directions with a resolution of 60 mesh points per h leading to a total grid of $2400 \times 600 \times 120$, i.e., a total of $172,800,000$ grid points. The CFL (Courant-Friedrichs-Lewy) number was set to be equal to 0.3 for the worst case resulting in a time-step of about 180 ns in the data collection phase.

The simulation was run on 800 CPUs on the supercomputers Beskow at PDC Center for High Performance Computing and Tetralith at National Supercomputer Center (NSC), for a total of about 330 h (including the time for the startup phase of the flow and the data collection), resulting in a total of 264,000 core-hours.

3.2 Boundary Conditions. A periodic boundary condition is applied in the spanwise direction, a convective outflow boundary condition [38] at the outlet, and a no-slip (stationary wall) condition for all walls.

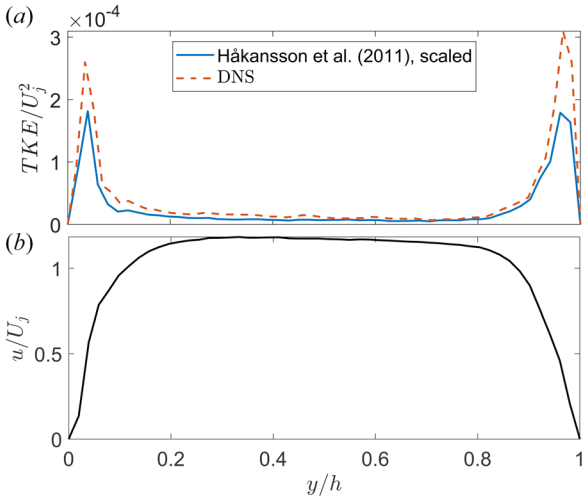

Fig. 2 (*a*) Mean TKE profiles and (*b*) mean streamwise velocity profiles, at the inlet for the PIV experiments of [2] and current DNS study

Modeling the inlet boundary condition to resemble the industrially relevant flow presents some special challenges. PIV measurements on HPH valve-geometries have shown the fluid exiting the narrow gap (i.e., entering the outlet chamber) having a skewed, not fully developed turbulent profile with high turbulent kinetic energy confined to the shear layers [2], see Fig. 2. These conditions at the inlet will influence the flow, at least for some gap heights inside the domain [2], and thus, great care is taken to impose a boundary condition on the DNS model that captures the conditions of the HPH. Several different inlet boundary conditions were reviewed and compared in preliminary investigations, aiming to reproduce both the trend in velocity and TKE profiles from the experiments. The best compromise was achieved by modeling the inlet with a combination of the experimentally obtained PIV data and anisotropic synthesized turbulent fluctuations [39–41]. What follows are taken into account in implementing the method:

(1) The mean streamwise velocity profile used is the one obtained from the PIV experiments [2], while the spanwise and wall-normal velocity components are set to zero.
(2) Synthetic fluctuations are generated at each simulation time-step using the anisotropic fluctuations method. Details of the method can be found in the original papers [39–41]. The three model parameters are set by combining the recommendations by Davidson [42] with preliminary results on a low-resolution channel:
   (a) *Entrance integral length scale* (L_t), was set to 0.04h, corresponding to 13% of the inlet boundary layer thickness (it is generally recommended to be at approximately 11% of the inlet boundary layer thickness).
   (b) *Baseline amplitude of fluctuations* (u_p). Following the recommendations [42], these should be $1.5 - 2.25$ times the shear velocity. The shear velocity is estimated to be 0.86 m/s at $Re = 2057$ using a preliminary DNS of a channel. Combined with a factor of 2.2, this resulted in $u_p = 1.892$ m/s.
   (c) *Time filtering and turbulent time scale* (τ). The fluctuations $u'_{i_{\text{uncorr}}}$ are generated at each time-step as described by Davidson and Billson [39], where index i designates the velocity component direction and index "uncorr" indicates that the generated fluctuations are not correlated in time. A time filtering was used to create a time-correlation for the generated fluctuations where $(u'_i)^m = a(u'_i)^{m-1} + b(u'_{i_{\text{uncorr}}})^m$ with $a = \exp(-\Delta t/\tau)$,

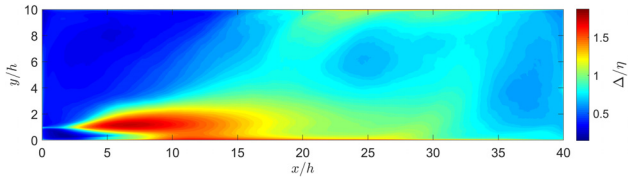

Fig. 3 Contour of Δ/η

$b = \sqrt{1-a^2}$, m is the time-step index, u_i' is the fluctuation generated at the specified time-step. The turbulence time scale τ scales with L_t/U_j to obtain values of $a = 0.995$ and $b = 0.104$. Finally, $(u_i')^m$ is the velocity fluctuation generated at time-step m, correlated with velocity fluctuations in time.

(3) Before adding the synthetic fluctuations to the PIV-obtained averages, they were scaled in order to obtain a TKE profile similar to the PIV results, $u'_{i_{\text{scaled}}} = u_i' \times \sqrt{\frac{2}{3}k}$ where k is the local turbulent kinetic energy from the PIV measurements.

However, PIV results of the TKE profile at the inlet boundary were only available for a substantially higher Reynolds number, hence the experimental profile first needed to be scaled. An appropriate scaling can be obtained from the relationship between bulk and shear velocities through the skin friction coefficient, $C_f = \frac{\tau_{\text{wall}}}{\frac{1}{2}\rho U_j^2} = \frac{u_\tau^2}{\frac{1}{2}U_j^2}$.

From the values of the shear velocities, the results of Refs. [43] and [44] are used to relate u_τ to peak RMS velocities. This resulted in a scaling factor for translating the TKE profiles from the PIV to the DNS inlet

$$\frac{k_{\text{Re}=2057}}{k_{\text{Re}=27000}} = \left(\frac{0.0573}{0.835}\right)^2 = 0.0047$$

Figure 2 compares the averaged TKE profiles at the inlet of the domain as obtained by the described boundary condition method, to the PIV-data from Ref. [2]. As seen in the figure, the TKE profile shows similar boundary layer peaks as the experimental data but at somewhat higher levels. The higher peak values are partly due to the fact that the spanwise contribution to the TKE was not considered in the 2D PIV study of Ref. [2]. Figure 2(*b*) shows the streamwise velocity profile from the PIV study which is used as the inlet velocity profile for the current study.

In summary, the inlet boundary generation method reproduces the main features of the inlet of the industrially relevant device, but not the details. This is due to the fact that the boundary condition method used for triggering turbulence requires some distance from the inlet to develop physical turbulence. Thus, care should be taken when interpreting the DNS data from the regions closest to the inlet. Further, into the domain, the turbulence generated by the shear layer between jet and recirculation zone, and with the wall is expected to dominate the flow. Thus, in the main region of interest in this study ($10 < x/h < 20$) the differences close to the inlet are not expected to significantly influence the results.

3.3 Mesh Resolution. As a requirement for a DNS study, the grid resolution (Δ) should be in the order of the Kolmogorov scale ($\Delta/\eta = O(1)$). The ratio of the grid resolution Δ (same in all directions) and the Kolmogorov scale η is illustrated in Fig. 3. The largest ratio found is 1.88 inside the jet outer shear layer. In other parts of the domain, this ratio is around 1 or less, indicating a sufficient mesh resolution. Another criterion proposed by Eswaran and Pope [45] is to keep the value of $\kappa_{\max}\eta$ above unity, where $\kappa_{\max}$ is the wavenumber corresponding to the largest mesh size. The results show that the worst-case close to the inlet has a value of $\kappa_{\max}\eta > 2.77$.

3.4 Validation of Spanwise Domain Length. The spanwise domain size, L_z, should be kept short to reduce the computational cost, but large enough to capture the relevant flow scales, i.e., the integral length. To validate that the spanwise distance is enough for the current simulation, the two-point correlations of fluctuating velocities are investigated in Fig. 4 on spanwise lines. The autocorrelation functions reaching zero at the critical points inside the shear layer indicates that a sufficient L_z is used. Figure 4 shows that this is achieved at most of the investigated locations within the jet (i.e., in the positions of main interest for the study). As seen in Fig. 4, the autocorrelation function does not reach zero at positions further downstream, but these positions are of less interest for discussing breakup. The flow at these positions behaves closer to a two-dimensional flow where we have large 2D flow structures. Furthermore, the integral length scales are calculated to be in the range $0.24 - 0.65$h in the studied points, indicating that the flow structures corresponding to these points are merely responsible for the advection rather than for the breakup of the droplets.

3.5 Convergence and Data Collection for Averaging. The flow field was initialized with the velocity field from a previous DNS simulation with a simplified inlet condition (constant but same bulk mean velocity). The simulations were run for approximately 30 passage times, t_{pass} (where a passage time is defined as the time required by a fluid element traveling with the inlet velocity to traverse the streamwise distance L_x), and 1200 gap time, t_g (where gap time is defined as $t_g = h/U_j$). Figure 5 shows the running average of the streamwise velocity component at five different points in the domain (see Fig. 1(*b*)) during the startup phase.

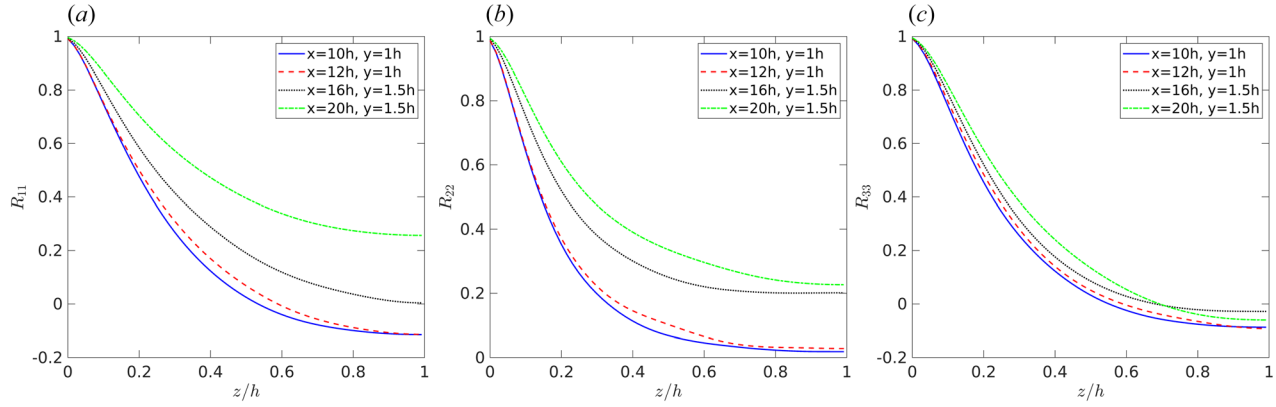

Fig. 4 Two-point correlations of: (*a*) streamwise, (*b*) wall-normal, and (*c*) spanwise fluctuating velocities on spanwise lines at different locations

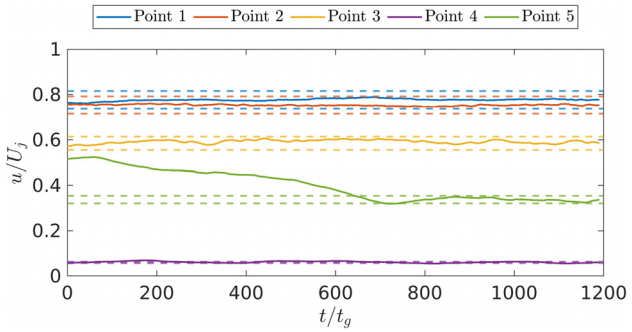

Fig. 5 Rolling average of streamwise velocity component at five different points

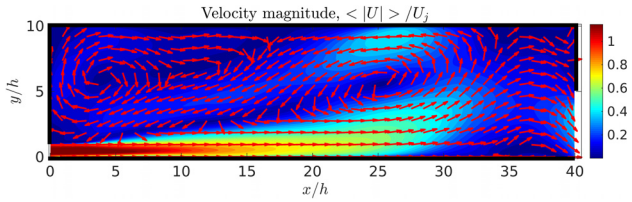

Fig. 6 Temporal and spatial (in spanwise direction) averaged velocity magnitude contour with velocity vectors

The window size was obtained by calculating the summation of absolute differences (SAD) as a function of different window sizes. SAD is the summation of absolute differences of the averaged signal with window size Δt_{win} and the actual signal. The window size after which SAD approaches a constant value is obtained to be $\Delta t_{\text{win}} = 0.03s$ $(640t_g)$ which is used as the window size for the running average.

The dashed lines show the 5% margin of the final averaged value for each corresponding point. The points positioned inside the jet (1, 2, and 3) are inside the 5% margin. This shows that changing the inlet condition from the previous simulation has not considerably changed the flow behavior inside the jet. However, in the points above the jet (points 4 and 5), no clear steady-state can be found. This behavior was also observed for the previous simulation (even after a considerably long simulation time of $528t_{\text{pass}}$ or $21120t_g$ corresponding to a physical time of 0.99 s). This indicates that there are slower dynamics influencing the flow in these regions, which however do no longer influence the jet. Investigations of the flow in these regions show that this slow-motion is caused by the periodic generation and exiting of large vortices (see continued discussion in Sec. 4.1), which makes it practically impossible to obtain a steady-state in these regions before starting data sampling.

The data sampling was run for a duration of 0.14 s (physical time), corresponding to $75t_{\text{pass}}$ or $3000t_g$. The sampling time was chosen long enough to obtain converged cumulative averages of all displayed turbulence statistics.

4 Results and Discussions

4.1 Flow Outline and General Behavior. Figure 6 illustrates the flow field using the contours of the averaged (temporally and in the spanwise direction) velocity magnitude, $|U|$ normalized by U_j. The red vectors show the direction of the flow in the xy-plane. The thick black lines indicate the position of the walls, with one wall covering half the outlet. The figure shows a high-velocity jet clinging to the lower wall, spreading as it extends downstream. Because of confinement, the jet gives rise to two vortex structures: one in the upper left corner, $(x = 4\text{h}, y = 6\text{h})$ just above the inlet, and the other right above the jet front at around $(x = 25\text{h}, y = 5.5\text{h})$. The significantly lower pressure (factor ~3) at the center of this second vortex indicates that this vortex is considerably stronger than the first one. A trapped vortex above the jet does exist in HPH outlet chambers (see Fig. 1(*a*)). Thus, the results in Fig. 6 show that the model geometry proposed in this study captures this important contribution to the turbulent jet dynamics.

As mentioned in Sec. 3.5, the velocities inside the jet, where breakup is expected to occur when drops are injected into the domain, converge to a steady flow field relatively fast. However, this is not the case for the points outside the jet (the two vortices) despite the long sampling times. Preliminary investigations show that this can be attributed to the dynamics of these large-scale eddies. Although these structures are outside the region of main interest for drop breakup, a brief discussion may be of interest to understand the flow from a macroscopic perspective and to discuss generalizability to industrial devices: Fig. 7 illustrates the dynamics of these large vortices based on contours on the middle spanwise plane (z = 1h), averaged over short time intervals $(\Delta t \approx 0.009s = 188t_g)$. The first panel (Fig. 7(*a*)) shows the same two main vortices as in the average contours, a strong

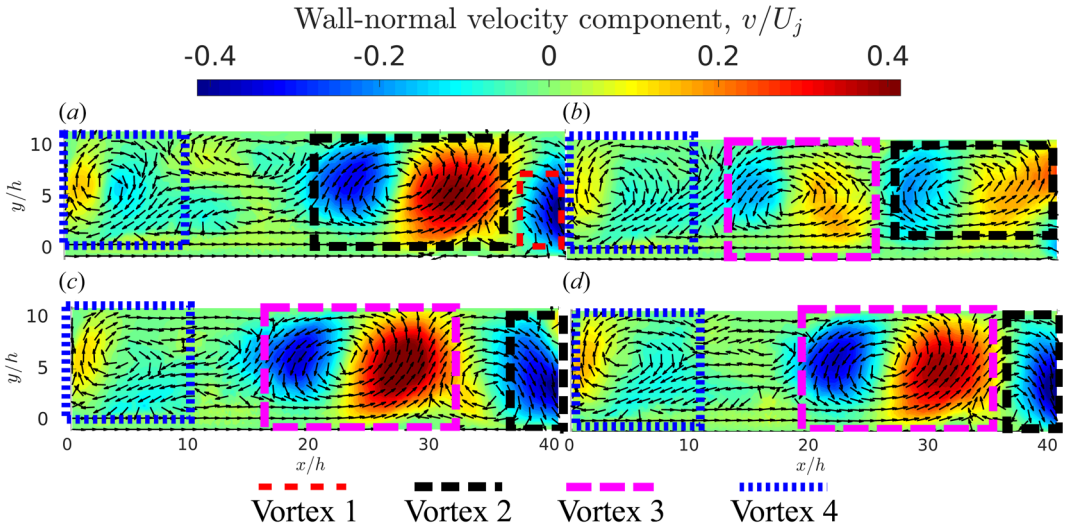

Fig. 7 Time-averaged wall-normal velocity contours in the middle plane (xy-plane) of the domain. Figure 7(*a*) is at $t = 0.061s$ $(1300t_g)$ after the flow startup and the next figures are consecutively taken with time difference of $0.009s$ $(192t_g)$.

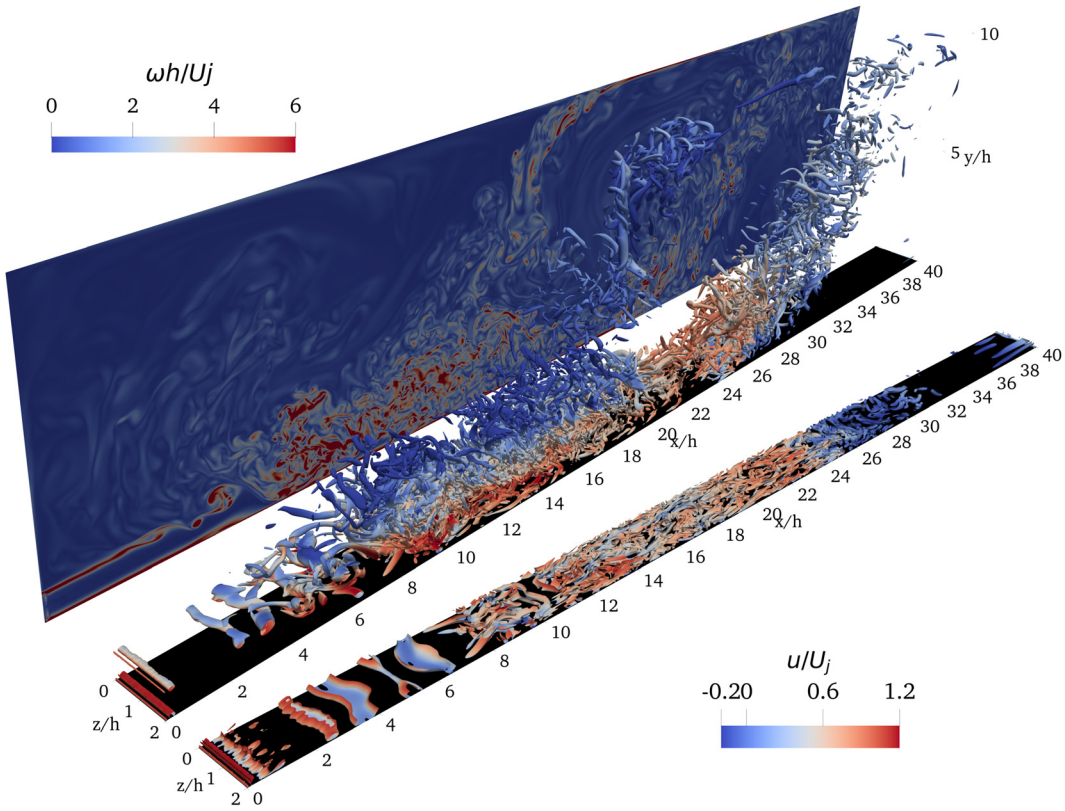

Fig. 8 Snapshot of vortex structures in the whole domain (inside the box in the middle) and close to the lower wall with $y < 0.2h$ (on the right) with instantaneous vorticity contour (on the left, behind the box)

counterclockwise eddy in the right part of the domain (henceforth referred to as vortex 2), and a weaker clock-wise eddy above the inlet (vortex 4). Moreover, part of a third vortex (vortex 1) can be seen just exiting the domain.

In the next part of the sequence (Fig. 7(*b*)), vortex 2 has been transported toward the exit, and a new vortex (vortex 3) can be seen to be generated at the tip of the jet behind vortex 2. Later, (Figs. 7(*c*) and 7(*d*)), vortex 2 is exiting and is being replaced by vortex 3 as the dominating structure in the right part of the domain. This process of continuous generation, transport, and exit of vortices persist over time and creates a periodicity in the flow outside of the main jet, which explains the difficulty in getting a converged average in the upper part of the domain (cf. Fig. 5).

The left vortex (vortex 4) is more persistent, being fed from the reverse flow above the jet body. However, investigating longer time intervals shows that this vortex also disappears and is replaced by a new vortex generated above the jet tip and moving to the left, however, over a substantially longer time scale.

The large-scale vortex dynamics are expected to be heavily dependent on the confinement of the flow. As discussed above, the wall jets found in industrial emulsification devices are confined but to a slightly lower degree than in the domain investigated here. Thus, care should be taken when attempting to generalize the results here above the jet.

4.2 Vortex Structures. In order to visualize the 3D vortex structures inside the domain, Q-criterion [46] isosurfaces are used. Figure 8 illustrates the instantaneous vortical structures in the entire domain and the structures close to the wall ($y < 0.2h$). The isosurfaces are colored based on the streamwise velocity component, u. Furthermore, contours of instantaneous normalized vorticity ($\omega h/U_j$) are illustrated for the plane $z = 0$. By looking at the 3D vortex structures, instabilities inside the shear layer seem to start at about $x = 2.5h$. These interact with each other and stronger and more consistent vortices start to appear after x approximatively 7 h. This is observed more clearly in the instantaneous vorticity contour plot. Here, vortices are more intense vortices mainly found for $7h < x < 18h$ (coinciding with the expected breakup region). This confirms that the highest deformation rates of the drops would occur before $x = 20h$ and the flow structures downstream of this location are not expected to be relevant for the breakup.

In order to visualize the vortex structures in the inner layer of the jet, only the structures below $y = 0.2h$ are illustrated. As observed, structures start to appear at about $x = 2.5h$. A transition length is observed between $x = 2.5h$ and $x = 8h$. After about $x = 8h$, more coherent turbulent structures start to develop. These observations are in agreement with the results of Ref. [31].

4.3 The Time-Averaged Jet. Drop breakup in HPHs is known to occur in the turbulent jet (approximately at $x = 10 - 20h$, [3,4]. Hence, the detailed behavior of the jet in this region is of special interest.

Figure 9 shows the streamwise time-averaged velocity profiles of the wall jet at five different locations downstream of the inlet ($x = 10h$, 12 h, 15 h, 18 h, and 20 h). The velocity has been normalized with the local maximum jet velocity (U_{max}) and the wall-normal lengths are normalized by $y_{1/2}$, where $y_{1/2}$ is the location at which the velocity is equal to $0.5U_{max}$. Between $x = 12h$ and $x = 20h$, the velocity profiles approximately collapse on a single line; smaller differences are observed, mainly above $y/y_{1/2} = 1.2$, indicating that an apparent self-similarity has developed after $x = 12h$. Further upstream, larger differences exist.

It is worth comparing the self-similar jet profiles to previous investigation of similar flows. A clear difference is found between the profiles in this study and Ref. [31] (data obtained at $x = 25h$), see Fig. 9. However, differences are expected since this study is on a wall jet with a significantly lower Reynolds number, which is expected to lead to a narrower boundary layer, even farther downstream of our investigated locations. A more relevant comparison

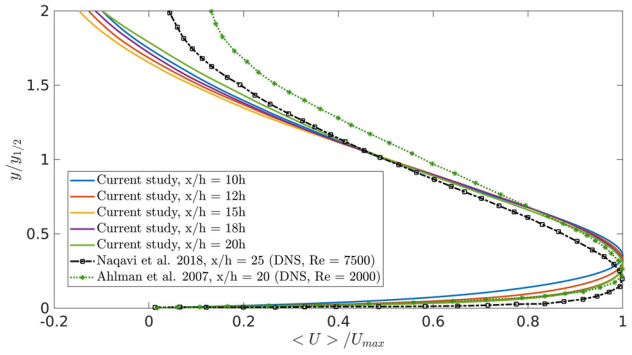

Fig. 9 Normalized average streamwise velocity profile in jet outer length scales

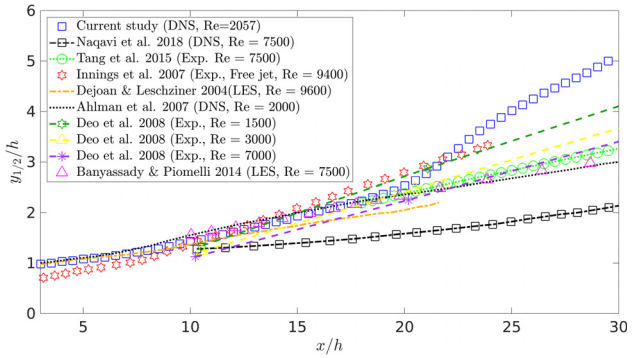

Fig. 10 $y_{1/2}/h$ as a function of the streamwise position x/h

is to the low-Re ($Re = 2000$) wall jet investigations of Ahlman et al. [29]. As seen in Fig. 9, these results are close to the results of the present study, up to $y/y_{1/2} = 0.69$. Above that, the profiles diverge. (Note that the difference between the present study and the results of Naqavi et al. [31] also increases further away from the wall). This is not surprising given the different setups. Both Ahlman et al. [29] and Naqavi et al. [31] study a pure wall jet and use a weak coflow above the jet to ensure that large-scale eddies forming at the shear layer leave the computational domain, i.e., they are not confined inside the domain as in our case, see Fig. 7. This leads to a substantial difference since we wish to include the confinement effects in order to mimic the flow interactions inside a homogenizer. Since Ahlman et al. [29] uses a higher coflow velocity ($U_c = 0.1U_j$) than [31] ($U_c = 0.06U_j$), a larger deviation is observed when compared to the former. The effect of this coflow can be readily seen in Fig. 9, in how it creates a positive streamwise velocity across the entire profile as compared to the back-flow due to the recirculation in the confined domain of the current study.

The spreading rate is an important characteristic describing the behavior of a jet. Figure 10 illustrates the jet width (measured as $y_{1/2}/h$) for different streamwise positions. The spreading rate is defined as the slope

$$S = \frac{dy_{1/2}(x)}{dx} \tag{1}$$

Three different regions can be seen in Fig. 10. First, before $x = 8$ h, the spreading rate is low ($S = 0.052$). Further downstream, between $x = 8$h and $x = 18$h, the spreading rate increases by around 92% and reaches $S = 0.1$. This behavior is also observed in experimental investigations of an HPH jet [1] where the spreading rate of the free jet doubled at 8 h from the gap exit of the high-pressure homogenizer (see Fig. 10). The shift of the jet behavior can be attributed to the interaction of the jet body with the recirculation eddies causing the flow structures in the shear layer to spread faster.

A third region can be observed, $x > 18$h, where the spreading rate increases to a value of 0.259, likely due to exit effects in the form of the strong upper right vortex starting to interact with the jet.

Since any drop breakup is expected to occur in a narrow region of the jet ($\sim 10 - 20$h), the second of these three regions is of principal interest and has been compared to previous investigations of similar wall jets in Fig. 10 and Table 2.

The most interesting comparison is with Ref. [29] which has a comparable Reynolds number to the present study, reporting a spreading rate of 0.068 for the developed wall-jet at $Re = 2000$. The higher spreading rate in our study is due again to recirculation eddies above the jet which are not present in a wall-jet with no flow confinement effect. The effect of these eddies can also explain why the two jets (our study and Ref. [29]) have a very similar behavior up to $x = 18$h, while they are noticeably different further downstream, $x > 18$h. The same can also be pointed out if we compare the results with the results of Banyassady and Piomelli [27].

The same observation is made when comparing to the results of Naqavi et al. [31] and Dejoan et al. [25], both obtained at considerably higher Reynolds numbers, with the effect that the spreading rate is higher before reaching the developed state. Deo et al. [21] showed that increasing the Reynolds number decreases the spreading of planar jets. Comparing their results for three different Reynolds numbers with our DNS results shows that the jet spreading of our case (Re = 2057) lies somewhere between the spreading for Re = 1500 and Re = 3000. This inverse relationship between the Reynolds number and the spreading rate justifies why we have

Table 2 Summary of the results for different studies

Study	Type[a]	Confinement L_y/h	U_c/U_j	Re_g	S	$U_{\max}$ decay $\frac{U_{\max}}{U_j} = A\left(\frac{x}{h}\right)^{\gamma}$
Current study	1	10	None	2057	0.052 ($x < 8h$) 0.100 ($x = 8h - 18h$) 0.259 ($x = 18h - 30h$)	$A = 1.199$, $\gamma = -0.0145$ ($x < 6h$) $A = 2.99$, $\gamma = -0.481$ ($x = 10h - 22h$) $A = 1785$, $\gamma = -2.47$ ($x = 25h - 30h$)
Ref. [29]	1	18	0.1	2000	0.068	NA
Ref. [31]	1	40	0.06	7500	0.065	$A = 3.55$, $\gamma = -0.4907$
Ref. [1]	2	60	None	9400	0.07 ($x < 8h$) 0.14 ($x > 8h$)	NA
Ref. [25]	1	10	0[b]	9600	0.0732 ($x > 10h$)	$A = 1.871$, $\gamma = -0.311$[b]
Ref. [47]	3	$Ly \gg h$	None	9600	0.0747[c]	$A = 5.15$, $\gamma = -0.6$
Ref. [23]	3	$Ly \gg h$	None	7500	0.0818[c]	$A = 3.442$, $\gamma = -0.482$
Ref. [27]	1	20	0[b]	7500	0.077($x > 10h$)[b]	$A = 1.967$, $\gamma = -0.329$[b]

[a]1: Confined wall jet, 2: Confined free jet, 3: Nonconfined wall jet.
[b]Instead of coflow, special boundary condition is applied to the upper wall.
[c]This is not reported by the study, but calculated from the available reported results.

higher spreading rates compared to other wall-jet studies with higher Reynolds numbers.

Another difference between the present study and previous investigations is the coflow used in some of the other works (see discussion above). One could argue that the coflow does not only remove the recirculation eddies above the jet, but also affects the behavior of the jet by pushing the flow toward the wall. This would lead to a lower spreading rate. As seen in Table 2, Studies not using this coflow setup or using a lower value for the coflow velocity display a behavior closer to our results in terms of jet spreading rate before $x = 20$h.

The jet maximum velocity, $U_{\max}$ is another important property of a turbulent wall jet. Figure 11, shows $U_{\max}$ as a function of streamwise position for the present study (blue solid line). The velocity is normalized by the jet bulk velocity U_j. The following power-law equation is commonly used for describing the streamwise decay of $U_{\max}$

$$\frac{U_{\max}}{U_j} = A\left(\frac{x}{h}\right)^{\gamma} \tag{2}$$

with constant A and γ. Several regions can be seen when inspecting Fig. 11. First, before $x = 6h$, $\gamma = -0.0145$ which marks a predeveloped jet; in the range $x = 6 - 10$h, a transition is observed. Downstream of $10\,h$, the jet behaves as a developed jet as it reaches a self-similar region, until $x = 22$h. The values of $\gamma = -0.481$ and $A = 2.99$ are obtained in this region. This corresponds to a substantially slower decay than that found in a radial wall jet (see comparison in Fig. 11), but compares well to the typical ranges reported in the literature for developed wall-jets [31,47], see Fig. 10 and Table 2. However, differences are observed which we believe are mainly due to the flow setup, i.e., reverse flow, and inlet conditions. Furthermore, for $x > 22$h, the decay rate is seen to change again, which is not observed in other studies on unbounded jet flows. This is due to the wall-normal flow confinement; since our interest is in the region before $x = 20$h, we do not investigate this in more detail.

4.4 Characterization of the Time-Averaged Turbulence. Obtaining an in-depth understanding of the spatial variations of Reynolds stresses and the dissipation rate of turbulent kinetic energy is of special importance since these are often described as directly controlling drop breakup in emulsification devices [48,49].

Figure 12 shows the three components of the velocity fluctuations in the form of contour plots in the jet region ($0 < x/h < 25$, $0 < y/h < 4$). The velocity fluctuation profiles at six different streamwise locations have been added to the figures. Both contours and profile values are normalized by the jet bulk velocity (U_j) and the maximum velocity locations and jet half-width ($y_{1/2}$) are depicted with purple triangles and black squares, respectively.

Figure 12(*a*) shows the streamwise velocity fluctuations. A high-intensity region is observed in the range $x = 5 - 11$h inside the shear layer. The profiles show two peaks, one in the inner layer and the other one in the shear layer (i.e., outer layer) of the jet. The inner layer peaks is at about $y^+ = 19 - 29$ for the main region of interest ($x/h = 10 - 20$). The peaks in the outer layer before $x/h = 14$ are at the vicinity of $y_{1/2}$, in the range $(0.76 - 0.8)\ y_{1/2}$. These locations closely correspond to the maximum velocity gradient, as expected.

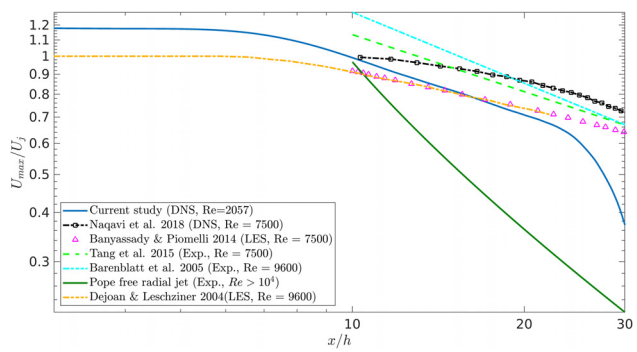

Fig. 11 U_{max}/U_j **as a function of the streamwise position** x/h

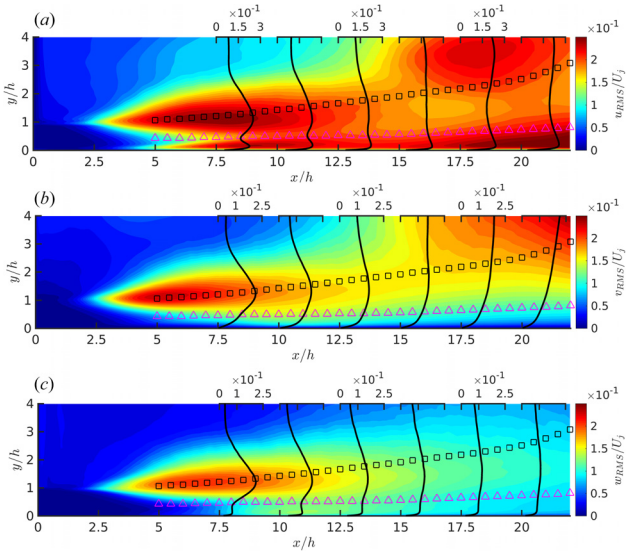

Fig. 12 Velocity fluctuation components contours and profiles at different streamwise locations: (*a*) streamwise velocity fluctuations u'_{RMS}/U_j, (*b*) wall-normal velocity fluctuations v'_{RMS}/U_j, and (*c*) spanwise velocity fluctuations w'_{RMS}/U_j

As seen in Fig. 12(*a*), a region of apparently high fluctuating velocities can also be seen above the jet at positions further downstream ($x/h > 14$). However, as discussed in the appendix, the slow dynamics of the flow structures in these regions, i.e., large time-scale differences compared to the expected breakup region inside the jet, makes these regions irrelevant for understanding drop breakup in these devices.

The wall-normal component of the velocity fluctuations is presented in Fig. 12(*b*). In the inner layer close to the wall, no peaks exist, leading to low values at the walls. This suggests high levels of anisotropy. For the spanwise fluctuations, local peaks exist until around $x = 10$h, after which this inner layer peak changes to a plateau. For wall-normal fluctuations, the peak values are also affected by the high TKE region as discussed for the streamwise fluctuations. Before $x = 14$h, the peaks in the outer layer are also located in the vicinity of the $y_{1/2}$ points, in the range $(0.87 - 0.93)\ y_{1/2}$. However, for the spanwise fluctuations, the outer peaks are not affected by the high TKE region above the jet and lie in the range $(0.62 - 0.86)$ of $y_{1/2}$ points in the streamwise range $x/h = 10 - 20$.

Figure 13 shows the contours of the normalized TKE values and profiles at different streamwise positions. Just as with the streamwise component, the peak in the inner layer occurs in the range $y^+ = 26 - 42$ for $x/h = 10 - 20$. The local minima

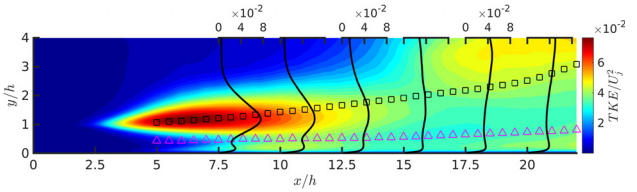

Fig. 13 TKE/U_j^2 Contours and profiles at different streamwise locations

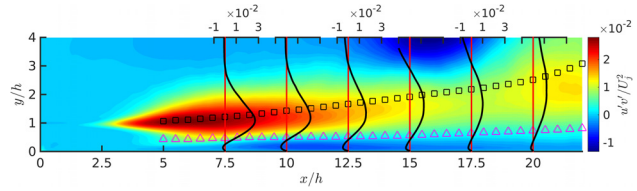

Fig. 14 Reynolds stress $u'v'/U_j^2$ Contours and profiles at different streamwise locations

between the two peaks are located closely to the locations of maximum velocity $U_{\max}$ and the outer layer peaks are in the range $(0.76-0.85)\ y_{1/2}$ for the streamwise locations before $x/h=15$. Downstream $x/h=15$, the outer layer peaks are again affected by the high TKE region as discussed for the streamwise and wall-normal fluctuations. Again, the high TKE region observed in the upper right corner is due to slow dynamics and its effect on the averaging process (as discussed in Appendix).

Figure 14 illustrates the contours and profiles at different streamwise positions of the normalized Reynolds stress $\langle u'v'\rangle/(U_j^2)$. The profiles show a negative peak in the vicinity of the wall at $y^+=15-17$ for $x/h=13-20$. The peaks in the outer layer are at locations comparable with those of the maximum fluctuation components being in the range $(0.78-0.86)$ $y_{1/2}$. Another observation is that the points where $\langle u'v'\rangle=0$ (vanishing Reynolds shear stress) are located in the range $y^+=41-50$. Due to the dominance of the production term for the Reynolds shear stress term $(-u_i'u_j'\frac{\partial \bar{u}_i}{\partial x_j}$, where $i\neq j)$ compared to the production terms of normal Reynolds stresses, negative productions of TKE are observed at small regions at the boundary layer at $x<8$h and other small parts of the domain (Fig. 19(*a*)). However, these negative values are negligible compared to the production values at other parts. This is consistent with the results of Ahlman et al. [29].

As mentioned above, the TKE dissipation rate is of special importance when characterizing the turbulence in an emulsification device since it is often assumed to determine breakup rates [50–52]. TKE dissipation rates in emulsification devices are still very poorly understood since it is difficult to estimate both using common RANS-CFD or 2D PIV (the two most prevalent methods used in previous studies).

Figure 15 illustrates the normalized TKE dissipation field with profiles at different streamwise locations calculated from the DNS. The general overview is in agreement to the cruder predictions in previous investigations: High dissipative regions are found close to the wall as observed also in typical channel flows. However, the majority of the dissipation takes place inside the shear layer with the relatively highest dissipation values extending in the streamwise direction from $x/h=3$ to 16 and $y/h=0.6-2.3$ in wall-normal direction. The maxima in the outer layer are found in the vicinity of the $y_{1/2}$ points.

From the perspective of a fluid element (or drop) traveling through the jet, the TKE dissipation rate on the center of the jet is of special interest. As seen in Fig. 15, the level increases from a low value at the inlet as the dissipation in the shear layer spreads inwards to the jet core and reaches its highest value of $7\times10^{-3}U_j^3/h$ at $x/h=11$, before decreasing again.

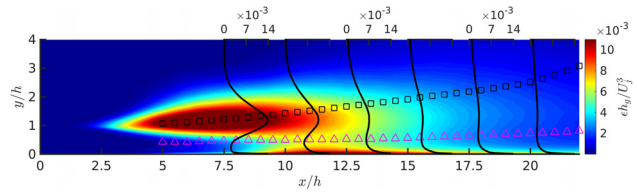

Fig. 15 Dissipation rate of *TKE*, $\epsilon h_g/U_j^3$ contours and profiles at different streamwise locations

The absolute level of TKE dissipation rate is especially difficult to determine using the previously available data (RANS-CFD and 2D PIV). The time-averaged dissipation rate of TKE in Fig. 15 shows a maximum rate of about $0.01U_j^3/h$ in a region of $(5<x/h<10,\ 1<y/h<1.5)$ and the volume average across the region where breakup is expected to occur $(10<x/h<20,\ 0.5<y/h<2.5)$ is $0.004U_j^3/h$, this can be compared with the previously suggested scaling laws for HPHs, estimating the average TKE dissipation rate in the efficient breakup region to be $0.05-0.0125U_j^3/h$ [1,49], indicating that these crude scaling laws provide estimates of the right order of magnitude but overestimate the averages somewhat.

4.5 Energy Spectra. Further insight into the length-scales of the turbulent fluctuations can be obtained by the energy spectra. The energy content at different length-scales has been suggested to be important for predicting breakup [32,53].

The one-dimensional spanwise energy spectra of the streamwise velocity (E_{11}) are presented in Fig. 16. Figure 16(*a*) shows the energy spectra on a line connecting the local maximum velocity points $U_{\max}$ (purple triangle points in Fig. 13) in the range $x=8$h to $x=20$h. Figure 16(*b*), instead, illustrates the energy spectra on a vertical line at the streamwise position $x=12$h. In both figures, the $\kappa^{-5/3}$-behavior is reported to

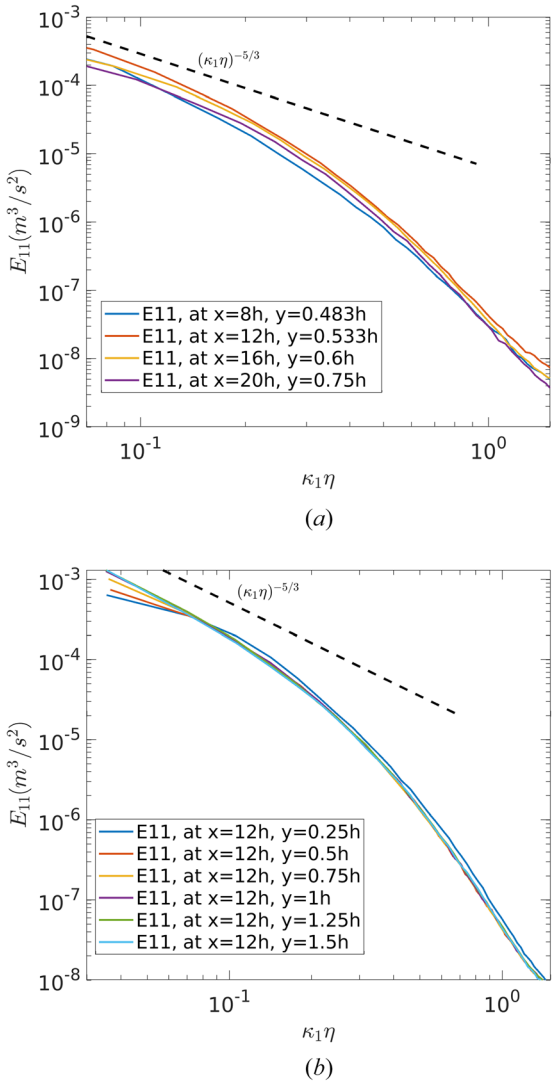

Fig. 16 One-dimensional spanwise energy spectra for streamwise velocity E_{11}: (*a*) On a line connecting $y_{1/2}$ points and (*b*) on a vertical line at $x=12h$

compare to the theoretical scaling in the inertial range. This can be observed in all data, with a clear dissipative range at wave numbers approaching the Kolmogorov microscale. However, due to the low Reynolds number ($\mathrm{Re}_\lambda < 100$ inside the shear layer), there is no clear separation of scales. This also affects the dissipative range of the spectra (at higher wavenumbers); in particular, we cannot identify a specific scale defining the dissipative range.

The spectra in Fig. 16 also allow a comparison between different locations. In Fig. 16(*a*) (showing the differences as a function of the streamwise distance), we can note an increase of the energy from the low levels at $x/h = 8$. Moving downstream to $x/h = 12$ shows an increase of the energy in all scales. However, moving further downstream shows decreased energy levels indicating the highest energy levels to occur around $x/h = 12$. Looking at different points at different wall-normal distances (Fig. 16(*b*)) does not suggest any significant changes in the energy levels.

Experimental investigations of HPH jets [2] have previously suggested a transfer of energy from larger to smaller eddies with increasing the distance from the gap exit , i.e., closer to the gap, higher proportion of the energy is contained in the larger scales, but at positions further downstream, a transfer of energy is observed from large to small scales leading to more energy being available to the smaller eddies. This effect cannot be seen in the current study.

5 Conclusions

A one-phase DNS investigation was carried out to study the turbulent flow in a confined wall jet, designed to mimic the flow in the region where breakup takes place in an HPH valve. This is the first DNS investigation of an emulsification device, thus making it possible to study the turbulence in these devices at a substantially higher level than in previous investigations.

The confinement creates two large-scale slowly moving vortices. The Jet spreading rate and maximum velocity decay resemble results from previous studies of wall jets at similar Reynolds numbers, when taking the effect of coflows into account.

High levels of Reynolds stresses and TKE are found in the wall shear layers, in particular in the outer shear layer where the jet interacts with the recirculation zone created by the confinement.

This study provides the first reliable estimation of TKE dissipation rates in a flow similar to that in an industrially relevant emulsification device, showing that the maximum level for a fluid element passing through the jet is obtained at a distance of $x/h = 11.3$ to be $6.7 \times 10^{-3} U_j^3/h$.

Acknowledgment

This study was financed by the Swedish Research council (VR), grant number 2018-03820 and Tetra Pak Processing Systems AB. The computations and data handling were enabled by resources provided by the Swedish National Infrastructure for Computing (SNIC) at PDC and NSC, partially funded by the Swedish Research Council through grant agreement no. 2018-05973.

Funding Data

- Swedish Research Council (VR) (Grant Nos. 2018-03820 and 2018-05973; Funder ID: 10.13039/501100004359).

Nomenclature

C_f = skin friction coefficient
d = initial drop size
E_{11} = spanwise one-dimensional energy spectrum of streamwise velocity
h = gap height
k = turbulent kinetic energy
L = integral length scale
L_x = domain streamwise length
L_y = domain wall-normal length
L_z = domain spanwise length
L_t = entrance (inlet) integral length scale
$\mathcal{P}$ = production rate of TKE
Re = Reynolds number
Re_λ = Taylor-scale Reynolds number
S = jet spreading rate
t_{pass} = flow passage time ($t_{\mathrm{pass}} = \frac{L_x}{U_j}$)
t_g = flow gap time ($t_g = \frac{h}{U_j}$)
U_j = gap bulk velocity
U_c = co-flow velocity
U_{max} = maximum local jet velocity
u_p = baseline amplitude of fluctuations
u_i' = velocity fluctuation components
u_τ = shear velocity
$y_{1/2}$ = jet half-maximum velocity location
y_+ = dimensionless wall distance
δ_{99} = asymptotic boundary layer thickness
Δ = grid resolution
Δt = time step
η = Kolmogorov micro scale
κ = wave-number
ρ = fluid density
τ = turbulent time scale
τ_{wall} = wall shear stress
ω = vorticity
uncorr = uncorrelated in time
scaled = scaled value
win = running average window
CFL = Courant–Friedrichs–Lewy number
DNS = direct numerical simulation
HPH = high-pressure homogenizer
LES = large eddy simulation
PIV = particle image velocimetry
SAD = summation of absolute differences

Appendix: Investigating the High Turbulence Levels in the Vortex Region

As discussed in connection to Fig. 7, two large but slow vortices are created above the jet due to the confinement in the wall-normal direction. The dynamics of these vortices are substantially slower than that of the turbulence in the main region of interest (inside the jet at $10 < x/h < 20$, $0 < y/h < 4$, where breakup of injected drops are expected to occur). Although, this is not expected to influence statistics collected inside the jet, but, it will lead to convergence issues in the time averaged velocity fluctuations, Reynolds stresses and TKE in the vortex region. This can be seen in Fig. 17 showing the contours of the TKE averaged across the entire data collection period. Note the high TKE region in the upper right corner. This is not a position where a high TKE would be expected since the time averaged gradients are not sufficiently high.

The cause of this observation can be understood from the dynamics studies in Fig. 7. The large vortex is slowly moving toward the exit (at the same time as it is being replaced by a newly

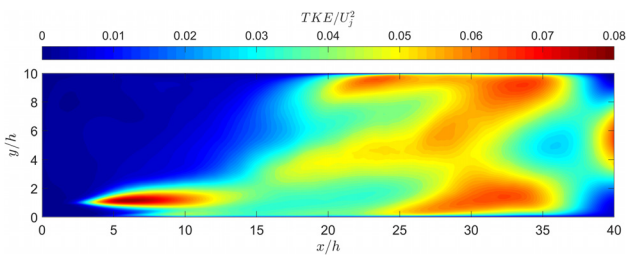

Fig. 17 Normalized TKE contour in the entire domain

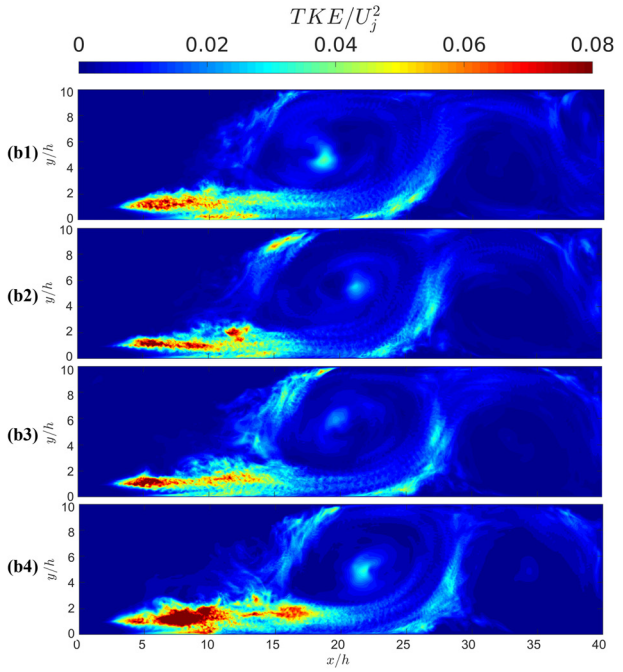

Fig. 18 Normalized TKE contours averaged in short time intervals $\Delta t = 0.0009s$ or $19.2t_g$

generated one). Performing the time average on the flow field, and particularly in this region, will appear as fluctuations when subtracting instantaneous average velocities from the temporal average which is mainly due to the movement-generation-disappearance process of these large vortices.

Furthermore, to illustrate the difference of the time scales compared to the turbulence in the shear layer, as well as showing that this is merely a consequence of temporal averaging, Fig. 18 shows a sequence of TKE contours averaged across short time intervals ($0.0009s$ or $19.2t_g$). In fact, the sequence b in Fig. 7 corresponds to the starting sequence b1 in Fig. 18. b2-b4 are consecutively averaged sequences with averaging time window $\Delta t = 0.0009s$. As seen in the figure, the high TKE regions downstream $x = 20h$ disappears. This proves that the time scales at these regions are significantly larger and not comparable to the turbulence time scales in the shear layer which are the most relevant for breakup.

Other arguments to rule out these turbulent regions as irrelevant structures to this study is to look at the production of TKE. Fig. 19(*a*) shows considerably small values of the production of TKE in the regions beyond the jet shear layer. Furthermore, Fig. 19(*b*) illustrates the eddy turn-over times (defined as the ratio of the gap height to the mean velocity magnitude). Due to the large separation of time scales and to show this large separation, the range of the colormap is considered up to 2×10^{-4} s and the monochromatic dark region outside the main jet body represent any value larger than this. The figure clearly shows the large difference in the eddy turn-over times inside the jet body and the shear layer with the other parts of the domain. Therefore, one could conclude that the high turbulence regions above the jet (except for a small region at $x = 25h$ and close to the upper wall) have entirely different dynamics compared to the regions of breakup.

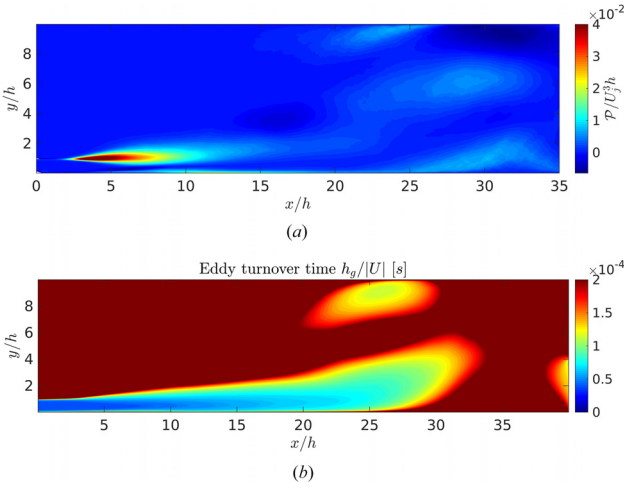

Fig. 19 (*a*) Production of TKE contour and (*b*) Eddy turnover time contour

References

[1] Innings, F., and Trägårdh, C., 2007, "Analysis of the Flow Field in a High-Pressure Homogenizer," Exp. Therm. Fluid Sci., **32**(2), pp. 345–354.
[2] Håkansson, A., Fuchs, L., Innings, F., Revstedt, J., Trägårdh, C., and Bergenståhl, B., 2011, "High Resolution Experimental Measurement of Turbulent Flow Field in a High Pressure Homogenizer Model and Its Implications on Turbulent Drop Fragmentation," Chem. Eng. Sci., **66**(8), pp. 1790–1801.
[3] Innings, F., and Trägårdh, C., 2005, "Visualization of the Drop Deformation and Break-Up Process in a High Pressure Homogenizer," Chem. Eng. Technol., **28**(8), pp. 882–891.
[4] Innings, F., Fuchs, L., and Trägårdh, C., 2011, "Theoretical and Experimental Analyses of Drop Deformation and Break-Up in a Scale Model of a High-Pressure Homogenizer," J. Food Eng., **103**(1), pp. 21–28.
[5] Kelemen, K., Gepperth, S., Koch, R., Bauer, H.-J., and Schuchmann, H. P., 2015, "On the Visualization of Droplet Deformation and Breakup During High-Pressure Homogenization," Microfluid. Nanofluidics, **19**(5), pp. 1139–1158.
[6] Raikar, N. B., Bhatia, S. R., Malone, M. F., McClements, D. J., and Henson, M. A., 2011, "Predicting the Effect of the Homogenization Pressure on Emulsion Drop-Size Distributions," Ind. Eng. Chem. Res., **50**(10), pp. 6089–6100.
[7] Maindarkar, S. N., Hoogland, H., and Henson, M. A., 2015, "Predicting the Combined Effects of Oil and Surfactant Concentrations on the Drop Size Distributions of Homogenized Emulsions," Colloids Surf. A: Physicochem. Eng. Aspects, **467**, pp. 18–30.
[8] Guan, X., Yang, N., and Nigam, K. D., 2020, "Prediction of Droplet Size Distribution for High Pressure Homogenizers With Heterogeneous Turbulent Dissipation Rate," Ind. Eng. Chem. Res., **59**(9), pp. 4020–4032.
[9] Mutsch, B., Preiss, F. J., Dagenbach, T., Karbstein, H. P., and Kähler, C. J., 2021, "Scaling of Droplet Breakup in High-Pressure Homogenizer Orifices. Part II: Visualization of the Turbulent Droplet Breakup," Chem Eng., **5**(2), p. 31.
[10] Solsvik, J., Tangen, S., and Jakobsen, H. A., 2013, "On the Constitutive Equations for Fluid Particle Breakage," Rev. Chem. Eng., **29**(5), pp. 241–356.
[11] Floury, J., Bellettre, J., Legrand, J., and Desrumaux, A., 2004, "Analysis of a New Type of High Pressure Homogeniser. a Study of the Flow Pattern," Chem. Eng. Sci., **59**(4), pp. 843–853.
[12] Steiner, H., Teppner, R., Brenn, G., Vankova, N., Tcholakova, S., and Denkov, N., 2006, "Numerical Simulation and Experimental Study of Emulsification in a Narrow-Gap Homogenizer," Chem. Eng. Sci., **61**(17), pp. 5841–5855.
[13] Håkansson, A., Fuchs, L., Innings, F., Revstedt, J., Trägårdh, C., and Bergenståhl, B., 2012, "Experimental Validation of $k'\varepsilon$ RANS-CFD on a High-Pressure Homogenizer Valve," Chem. Eng. Sci., **71**, pp. 264–273.
[14] Bakke, P., 1957, "An Experimental Investigation of a Wall Jet," J. Fluid Mech., **2**(05), pp. 467–472.
[15] Schwarz, W. H., and Cosart, W. P., 1961, "The Two-Dimensional Turbulent Wall-Jet," J. Fluid Mech., **10**(04), pp. 481–495.
[16] Myers, G. E., Schauer, J. J., and Eustis, R. H., 1963, "Plane Turbulent Wall Jet Flow Development and Friction Factor," ASME J. Basic Eng., **85**(1), pp. 47–53.
[17] Gartshore, I. S., and Newman, B. G., 1969, "The Turbulent Wall Jet in an Arbitrary Pressure Gradient," Aeronaut. Q., **20**(1), pp. 25–56.
[18] Bajura, R. A., and Szewczyk, A. A., 1970, "Experimental Investigation of a Laminar Two-Dimensional Plane Wall Jet," Phys. Fluids, **13**(7), pp. 1653–1664.
[19] Neale, D. H., 1971, "Experimental Study of Two-Dimensional Turbulent Wall Jet Development With and Without Longitudinal Free Stream Pressure Gradient," Doctoral dissertation, Georgia Institute of Technology, Atlanta, GA.
[20] Eriksson, J. G., Karlsson, R. I., and Persson, J., 1998, "An Experimental Study of a Two-Dimensional Plane Turbulent Wall Jet," Exp. Fluids, **25**(1), pp. 50–60.
[21] Deo, R. C., Mi, J., and Nathan, G. J., 2008, "The Influence of Reynolds Number on a Plane Jet," Phys. Fluids, **20**(7), p. 075108.
[22] Rostamy, N., Bergstrom, D. J., Sumner, D., and Bugg, J. D., 2011, "The Effect of Surface Roughness on the Turbulence Structure of a Plane Wall Jet," Phys. Fluids, **23**(8), p. 085103.
[23] Tang, Z., Rostamy, N., Bergstrom, D., Bugg, J., and Sumner, D., 2015, "Incomplete Similarity of a Plane Turbulent Wall Jet on Smooth and Transitionally Rough Surfaces," J. Turbul., **16**(11), pp. 1076–1090.
[24] Launder, B., and Rodi, W., 1979, "The Turbulent Wall Jet," Prog. Aerosp. Sci., **19**, pp. 81–128.

[25] Dejoan, A., and Leschziner, M. A., 2005, "Large Eddy Simulation of a Plane Turbulent Wall Jet," Phys. Fluids, **17**(2), p. 025102.
[26] Naqavi, I. Z., Tucker, P. G., and Liu, Y., 2014, "Large-Eddy Simulation of the Interaction of Wall Jets With External Stream," Int. J. Heat Fluid Flow, **50**, pp. 431–444.
[27] Banyassady, R., and Piomelli, U., 2014, "Turbulent Plane Wall Jets Over Smooth and Rough Surfaces," J. Turbul., **15**(3), pp. 186–207.
[28] Banyassady, R., and Piomelli, U., 2015, "Interaction of Inner and Outer Layers in Plane and Radial Wall Jets," J. Turbul., **16**(5), pp. 460–483.
[29] Ahlman, D., Brethouwer, G., and Johansson, A. V., 2007, "Direct Numerical Simulation of a Plane Turbulent Wall-Jet Including Scalar Mixing," Phys. Fluids, **19**(6), p. 065102.
[30] Pouransari, Z., Vervisch, L., Fuchs, L., and Johansson, A., 2016, "DNS Analysis of Wall Heat Transfer and Combustion Regimes in a Turbulent Non-Premixed Wall-Jet Flame," Flow, Turbul. Combust., **97**(3), pp. 951–969.
[31] Naqavi, I. Z., Tyacke, J. C., and Tucker, P. G., 2018, "Direct Numerical Simulation of a Wall Jet: Flow Physics," J. Fluid Mech., **852**, pp. 507–542.
[32] Håkansson, A., 2017, "Scale-Down Failed - Dissimilarities Between High-Pressure Homogenizers of Different Scales Due to Failed Mechanistic Matching," J. Food Eng., **195**, pp. 31–39.
[33] Phipps, L. W., 1982, "Homogenizing Valve Design and Its Influence on Milk Fat Globule Dispersion: I. low Rate of Flow ($100l/h$, $Re \leq 3000$)," J. Dairy Res., **49**(2), pp. 309–315.
[34] Rosti, M. E., and Brandt, L., 2017, "Numerical Simulation of Turbulent Channel Flow Over a Viscous Hyper-Elastic Wall," J. Fluid Mech., **830**, pp. 708–735.
[35] Rosti, M., De Vita, F., and Brandt, L., 2019, "Numerical Simulations of Emulsions in Shear Flows," Acta Mech., **230**(2), pp. 667–682.
[36] Picano, F., Breugem, W.-P., and Brandt, L., 2015, "Turbulent Channel Flow of Dense Suspensions of Neutrally Buoyant Spheres," J. Fluid Mech., **764**, pp. 463–487.
[37] Costa, P., 2018, "A FFT-Based Finite Difference Solver for Massively-Parallel Direct Numerical Simulations of Turbulent Flows," Comput. Math. Appl., **76**(8), pp. 1853–1862.
[38] Orlanski, I., 1976, "A Simple Boundary Condition for Unbounded Hyperbolic Flows," J. Comput. Phys., **21**(3), pp. 251–269.
[39] Davidson, L., and Billson, M., 2006, "Hybrid LES-RANS Using Synthesized Turbulent Fluctuations for Forcing in the Interface Region," Int. J. Heat Fluid Flow, **27**(6), pp. 1028–1042.
[40] Billson, M., Eriksson, L.-E., and Davidson, L., 2012, "Jet Noise Prediction Using Stochastic Turbulence Modeling," AIAA Paper No. 2003–3282.
[41] Davidson, L., and Peng, S.-H., 2013, "Embedded Large-Eddy Simulation Using the Partially Averaged Navier-Stokes Model," AIAA J., **51**(5), pp. 1066–1079.
[42] Davidson, L., 2007, "Using Isotropic Synthetic Fluctuations as Inlet Boundary Conditions for Unsteady Simulations," Adv. Appl. Fluid Mech., **1**, pp. 1–35.
[43] Tsukahara, T., Seki, Y., Kawamura, H., and Tochio, D., 2005, "DNS Turbulent Channel Flow at Very Low Reynolds Numbers," Paper presented at 4th International Symposium on Turbulence and Shear Flow Phenomena, TSFP 4, Williamsburg, VA, June 27–29, pp. 935–940.
[44] Bernardini, M., Pirozzoli, S., and Orlandi, P., 2014, "Velocity Statistics in Turbulent Channel Flow Up to $Re_\tau = 4000$," J. Fluid Mech., **742**, pp. 171–191.
[45] Eswaran, V., and Pope, S., 1988, "An Examination of Forcing in Direct Numerical Simulations of Turbulence," Comput. Fluids, **16**(3), pp. 257–278.
[46] Hunt, J., Wray, A., and Moin, P., 1988, "Eddies, Streams, and Convergence Zones in Turbulent Flows," Proceedings of the summer program, Report CTR-S88, NASA Stanford center for turbulence research, 1988, pp. 193–208.
[47] Barenblatt, G. I., Chorin, A. J., and Prostokishin, V. M., 2005, "The Turbulent Wall Jet: A Triple-Layered Structure and Incomplete Similarity," Proc. Natl. Acad. Sci., **102**(25), pp. 8850–8853.
[48] Walstra, P., and Smulders, P. E. A., 1998, "Emulsion Formation," Modern Aspects of Emulsion Science, B. P. Binks, ed., The Royal Society of Chemistry, Cambridge, UK, pp. 56–99.
[49] Mohr, K.-H., 1987, "High-Pressure Homogenization. part i. liquid-Liquid Dispersion in Turbulence Fields of High Energy Density," J. Food Eng., **6**(3), pp. 177–186.
[50] Liao, Y., and Lucas, D., 2009, "A Literature Review of Theoretical Models for Drop and Bubble Breakup in Turbulent Dispersions," Chem. Eng. Sci., **64**(15), pp. 3389–3406.
[51] Solsvik, J., Skjervold, V. T., and Jakobsen, H. A., 2017, "A Bubble Breakage Model for Finite Reynolds Number Flows," J. Dispersion Sci. Technol., **38**(7), pp. 973–978.
[52] Lasheras, J. C., Eastwood, C., Martínez-Bazán, C., and Montañés, J. L., 2002, "A Review of Statistical Models for the Break-Up of an Immiscible Fluid Immersed Into a Fully Developed Turbulent Flow," Int. J. Multiphase Flow, **28**(2), pp. 247–278.
[53] Bagkeris, I., Michael, V., Prosser, R., and Kowalski, A., 2021, "Modeling Drop Breakage Using the Full Energy Spectrum and a Specific Realization of Turbulence Anisotropy," AIChE J., **67**(7), p. e17201.